APPLIED PHYSICS

Deformation of an inner valence molecular orbital in ethanol by an intense laser field

Hiroshi Akagi*, Tomohito Otobe*, Ryuji Itakura*

Valence molecular orbitals play a crucial role in chemical reactions. Here, we reveal that an intense laser field deforms an inner valence orbital (10a′) in the ethanol molecule. We measure the recoil-frame photoelectron angular distribution (RFPAD), which corresponds to the orientation dependence of the ionization probability of the orbital, using photoelectron-photoion coincidence momentum imaging with a circularly polarized laser pulse. Ab initio simulations show that the orbital deformation depends strongly on the laser field direction and that the measured RFPAD cannot be reproduced without taking the orbital deformation into account. Our findings suggest that the laser-induced orbital deformation occurs before electron emission on a suboptical cycle time scale.

INTRODUCTION

Molecular orbital (MO) shape plays a crucial role in chemical reaction dynamics and is described by theories such as the frontier orbital (*1*) and Woodward-Hoffmann rules (*2*). Similarly, in intense laser–induced molecular dynamics, MO shape is known to be important, particularly in tunnel ionization (*3*, *4*). Tunnel ionization is a crucial initial step of successive dynamical processes, leading to high-harmonic generation, dissociative ionization, and multiple ionization. In the past two decades, orientation dependence of tunnel ionization probabilities has been studied mainly for small molecules composed of two or three atoms (*5*–*7*). These studies have shown that the shape of an MO from which an electron tunnels strongly affects the orientation dependence of the ionization probability. Hence, the ionization probability as a function of molecular orientation is measured to image the MO shape. This molecular scanning tunnel microscopy (STM) (*8*) has revealed that laser-induced tunneling occurs not only from the highest-occupied MO (HOMO) but also from inner valence orbitals (*9*). Inner valence orbitals play a crucial role in intense-field chemistry.

In addition to the contribution of multiple MOs (*9*–*11*), laser-induced deformation of HOMOs has been studied in tunnel ionization. Simulations including HOMO deformation agree well with the measured angular dependence of ionization probability for CO_2 (*12*) and with high-harmonic spectra from N_2 (*13*). Experimentally, high-harmonic spectroscopy with the aid of ab initio simulation has revealed that degenerate HOMOs in spatially oriented CH_3F are deformed by intense laser fields, which remove the degeneracy (*14*). The contribution of unoccupied MOs such as Rydberg orbitals was also suggested for dissociative ionization of hydrocarbon molecules (*15*). There is also evidence that intense laser fields modify the electronic structure of ionized molecules (*16*, *17*). In this study, we demonstrate laser-induced MO deformation of an inner valence orbital in a neutral molecule. Photoionization from an inner valence orbital is essential to creating electronically excited ions, which is necessary for many molecules to dissociate (*18*–*21*). For efficient control of laser-driven dissociative ionization, it is important to deepen our understanding of electronic dynamics of inner valence orbitals.

Kansai Photon Science Institute, National Institutes for Quantum and Radiological Science and Technology (QST), 8-1-7 Umemidai, Kizugawa, Kyoto 619-0215, Japan. *Corresponding author. Email: akagi.hiroshi@qst.go.jp (H.A.); otobe.tomohito@qst.go.jp (T.O.); itakura.ryuji@qst.go.jp (R.I.)

Ethanol is an ideal molecule for exhibiting MO deformation in a strong laser field. Ethanol has rather low symmetry (the point group *Cs*) with its symmetry plane including an O atom and two C atoms as shown in Fig. 1A. Hence, all MOs of ethanol are classified in two irreducible representations: a′ and a″. The energy levels of the four inner valence MOs, 10a′ (HOMO-1), 2a″ (HOMO-2), 9a′ (HOMO-3), and 8a′ (HOMO-4), lie within 3 eV of each other in the field-free situation (*22*), and three of the four MOs have a′ symmetry, as illustrated in the inset of Fig. 1A. In our experiment, we used a circularly polarized laser field with an intensity of $I_0 = 8 \times 10^{13}$ W/cm^2. The electric field of $E = 1.7 \times 10^{10}$ V/m creates a slope with an energy difference of about 6 eV for a distance of ~3.5 Å, which corresponds to the size of ethanol (Fig. 1A). This difference is larger than the energy range of the three a′ MOs in the field-free situation. Therefore, the laser field should induce strong mixing of these MOs. In addition, a previous photoelectron-photoion coincidence (PEPICO) measurement with a He lamp (He *I* at 21.2 eV) showed that electron emission from the inner valence MOs results in the formation of different fragment ions (*23*). This means that identifying fragment ion species allows us to identify the MO that has an electron hole just before the ethanol cation dissociates (*18*, *19*, *21*).

RESULTS AND DISCUSSION

First, we show theoretically that 10a′ (HOMO-1) in ethanol is deformed by a circularly polarized intense laser field ($I_0 = 8 \times 10^{13}$ W/cm^2 and $E = 1.7 \times 10^{10}$ V/m) during one cycle of the electric (***E***) field (Fig. 1A). The field-free MO 10a′ ($\Psi_{10a'}$), shown at the center of Fig. 1A, is composed mainly of the lone pair on the O atom and the C—C σ bond. We calculate the 10a′ orbitals in the ***E***-field with density functional theory (DFT). The deformed orbital shapes $\Upsilon_{10a'}(\Phi)$ are drawn around field-free $\Psi_{10a'}$ in Fig. 1A, where the ***E***-field is parallel to the *Cs* symmetry plane with the angle Φ between the ***E***-field direction and the C—C axis. As described later, our DFT calculation shows that the ionization occurs dominantly when the ***E***-field is parallel to the *Cs* symmetry plane. Thus, we focus on the ***E***-field being parallel to the symmetry plane. In the direction $\Phi = -22.5°$ (the CH_3 side), $\Upsilon_{10a'}$ ($\Phi = -22.5°$) is similar to field-free 9a′ ($\Psi_{9a'}$) shown in Fig. 1B. In the other directions, the deformed MO $\Upsilon_{10a'}(\Phi)$ exhibits only slight differences from field-free $\Psi_{10a'}$. Nevertheless, $\Upsilon_{10a'}(\Phi)$ expands in the direction opposite to the ***E***-field. These deformations of 10a′ occur on a suboptical cycle time scale of the circularly polarized laser pulse, as

illustrated in Fig. 1A. The field-deformed MO $\Upsilon_{10a'}(\Phi)$ can be described as a linear combination of the neighboring a′ MOs, $\Psi_{10a'}$ (HOMO-1), $\Psi_{9a'}$ (HOMO-3), and $\Psi_{8a'}$ (HOMO-4), as shown in Fig. 1B. When the ***E***-field is not parallel to the C_S symmetry plane, 10a′ can be mixed with 3a″ (HOMO) and 2a″ (HOMO-2), as well as 9a′ and 8a′, and the mixing between a′ and a″ orbitals is included in our calculation.

The deformation from $\Psi_{10a'}$ to $\Upsilon_{10a'}(\Phi)$ in the ***E***-field affects angular dependence of the ionization probability. In our experiment, we applied molecular STM to ethanol in a circularly polarized laser field ($\lambda \sim 795$ nm, $\Delta\tau \sim 60$ fs, and $I_0 \sim 8 \times 10^{13}$ W/cm^2) (*9*, *24*). We used a partially deuterated ethanol sample, CH_3CD_2OH, to avoid ambiguity in the mass assignment caused by producing different fragment ions with the same mass. An unaligned ethanol molecule was singly ionized in the circularly polarized intense laser field, and three-dimensional momentum vectors of the electron ($\vec{p}_{ele}$) and ion ($\vec{p}_{ion}$) produced were measured in coincidence with two position-sensitive detectors (Fig. 2A). Here, we focused on CD_2OH^+ [mass/charge ratio (*m*/*z*) = 33] production because the previous PEPICO measurement with a He lamp found that CD_2OH^+ is produced by electron emission from the 10a′ MO (HOMO-1) (*23*). In the circularly polarized intense laser field, the freed electron drifts perpendicularly to the ***E***-field direction at the moment of tunneling (*25*). The recoil direction of the CD_2OH^+ ion reflects the orientation of the parent molecule just before dissociation. Thus, the recoil-frame photoelectron angular distribution (RFPAD) for the CD_2OH^+ production channel in the circularly polarized laser field was derived with respect to the CD_2OH^+ recoil vectors (fig. S1C). The RFPAD shows preferential electron tunneling from the CH_3 side of CH_3CD_2OH (Fig. 2B).

To understand the experimental RFPAD, we simulated the angular dependence of the tunnel ionization probability using DFT (*4*). Figure 3A is the simulated ionization probability $W_{10a'}(\Phi, \Theta)$ of $\Upsilon_{10a'}(\Phi, \Theta)$ as a function of the ***E***-field direction (Φ, Θ) defined in the inset of Fig. 3A. The two-dimensional map of $W_{10a'}(\Phi, \Theta)$ shows the maximum at (Φ, Θ) = (157.5°, 90°). In other words, an electron in 10a′ tunnels preferentially from the CH_3 moiety as illustrated in Fig. 3D; thus, it is somewhat similar to the RFPAD measured for the CD_2OH^+ channel (Fig. 2B).

To evaluate the effect of MO deformation on tunnel ionization, we simulated the ionization probability $W^0_{10a'}(\Phi, \Theta)$ of the field-free MO $\Psi_{10a'}$, as shown in Fig. 3B. Comparing $W^0_{10a'}(\Phi, \Theta)$ with $W_{10a'}(\Phi, \Theta)$

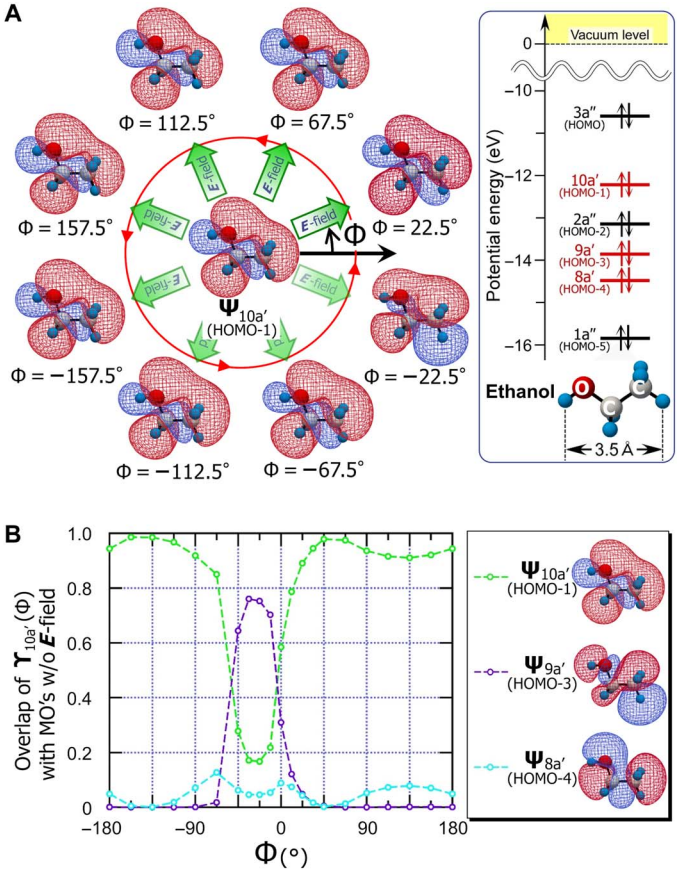

Fig. 1. MO deformation induced by a laser electric field. (**A**) Density functional theory (DFT)–calculated 10a′ (HOMO-1) structures of ethanol in an electric field with strength of 1.7×10^{10} V/m (corresponding to a circularly polarized laser field at an intensity of 8×10^{13} W/cm^2) as a function of field direction. The electric field direction is set parallel to the *Cs* symmetry plane and defined by the angle Φ from the C—C axis of ethanol. Isosurface plots of the MOs $\Upsilon_{10a'}(\Phi)$ in the electric field with cutoff values of 0.025 (blue) and –0.025 (red) are drawn around that of the field-free MO ($\Psi_{10a'}$). Inset: Energy level diagram of the field-free MOs in ethanol. The red and black levels have a′ and a″ symmetries, respectively. (**B**) Overlap populations $|\langle\Psi_i \mid \Upsilon_{10a'}(\Phi)\rangle|^2$ of $\Upsilon_{10a'}(\Phi)$ with the field-free MOs $\Psi_{8a'}$, $\Psi_{9a'}$, and $\Psi_{10a'}$ as functions of angle Φ.

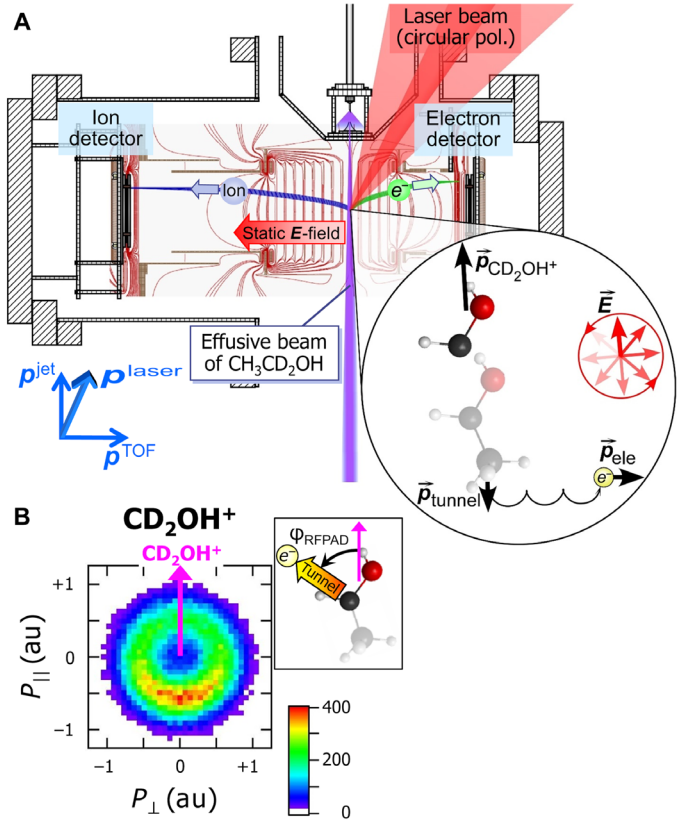

Fig. 2. Recoil-frame photoelectron momentum measurements. (**A**) Sketch of relations between the electron tunneling direction ($\vec{p}_{tunnel}$), final photoelectron momentum ($\vec{p}_{ele}$), recoil momentum of the CD_2OH^+ ion ($\vec{p}_{CD_2OH^+}$), and ***E***-field direction ($\vec{E}$) of the circularly polarized (circular pol.) laser field in the experimental setup. TOF, time of flight. (**B**) Recoil-frame photoelectron momentum distribution for the CD_2OH^+ channel. The arrow in the image indicates the recoil direction of the fragment ion.

clarifies the effect of MO deformation. The ionization probability $W_{10a'}(\Phi, \Theta)$ of field-free $\Psi_{10a'}$ has its maximum at $(\Phi, \Theta) = (-112.5°, 90°)$, where the electron tunnels from the lone pair on the O atom. The probability $W_{10a'}(\Phi, \Theta)$ of $\Upsilon_{10a'}(\Phi, \Theta)$ in the ***E***-field does not have any peaks around the direction $(\Phi, \Theta) = (-112.5°, 90°)$ (green dashed square in Fig. 3A) but has its maximum at $(\Phi, \Theta) = (157.5°, 90°)$ (pink dashed square), corresponding to electron tunneling from the CH_3 moiety. The change in the direction of maximum ionization probability can be explained by the substantial contribution of $\Psi_{8a'}$ to $\Upsilon_{10a'}(\Phi, \Theta)$, as shown in Fig. 3 (C and D). The MO $\Upsilon_{10a'}(\Phi, \Theta)$ in the ***E***-fields pointing to $(\Phi, \Theta) = (-112.5°, 90°)$ and $(157.5°, 90°)$ can be expressed as a linear combination of $\Psi_{10a'}$ and $\Psi_{8a'}$, which enlarges the lobe around the CH_3 moiety owing to the constructive overlap and shrinks the lone pair on the O atom owing to the destructive overlap. The deformation of 10a′ enhances electron tunneling from the CH_3 moiety and suppresses that from the lone pair on the O atom, as shown in Fig. 3 (C and D). In the ***E***-field pointing to $(\Phi, \Theta) = (-22.5°, 90°)$, $\Upsilon_{10a'}(\Phi, \Theta)$ indicates the strong mixing with $\Psi_{9a'}$ (Fig. 1B). However, the ionization probability shows only a slight increase in this direction, implying that the mixing with $\Psi_{9a'}$ does not cause a large spread of 10a′ MO in the direction opposite to the ***E***-field.

The experimental RFPAD for the CD_2OH^+ channel (Fig. 2B) gives evidence of MO deformation. To compare the experimental and simulated results, we derived the theoretical RFPADs from the two-dimensional maps of $W_{10a'}(\Phi, \Theta)$ and $W^0_{10a'}(\Phi, \Theta)$ shown in Fig. 3 (A and B). Here, the electron was assumed to tunnel in the opposite direction of the ***E***-field with an angular uncertainty of ±16°, which was estimated from the out-of-plane photoelectron angular distribution with respect to the polarization plane (fig. S3). For the fragment ion emission, we applied the axial recoil approximation. The RFPAD $\Omega_{10a'}(\varphi_{RFPAD})$ derived from $\Upsilon_{10a'}(\Phi, \Theta)$ in the ***E***-field has a peak at $\varphi_{RFPAD} \sim 180°$ (green line in Fig. 4A), showing the preferential electron tunneling from the CH_3 moiety. This agrees with the experimental RFPAD (pink line in Fig. 4A). Nevertheless, the theoretical RFPAD has a minimum at $\varphi_{RFPAD} \sim 90°$, which we did not observe in the experimental RFPAD. We attribute this discrepancy to the electron tunneling from 3a″ (HOMO), followed by the subsequent electronic excitation to the first electronically excited $1\,^2A'$ state [an electron hole in 10a′ (HOMO-1)] of the ethanol cation. This stepwise process also produces the CD_2OH^+ ion as illustrated in Fig. 4C (*18*, *19*, *21*).

To describe electronic excitation in intense laser fields, perturbative photoabsorption is not appropriate. As illustrated in Fig. 1A, the MO in neutral ethanol varies adiabatically as the ***E***-field rotates. In nonresonant

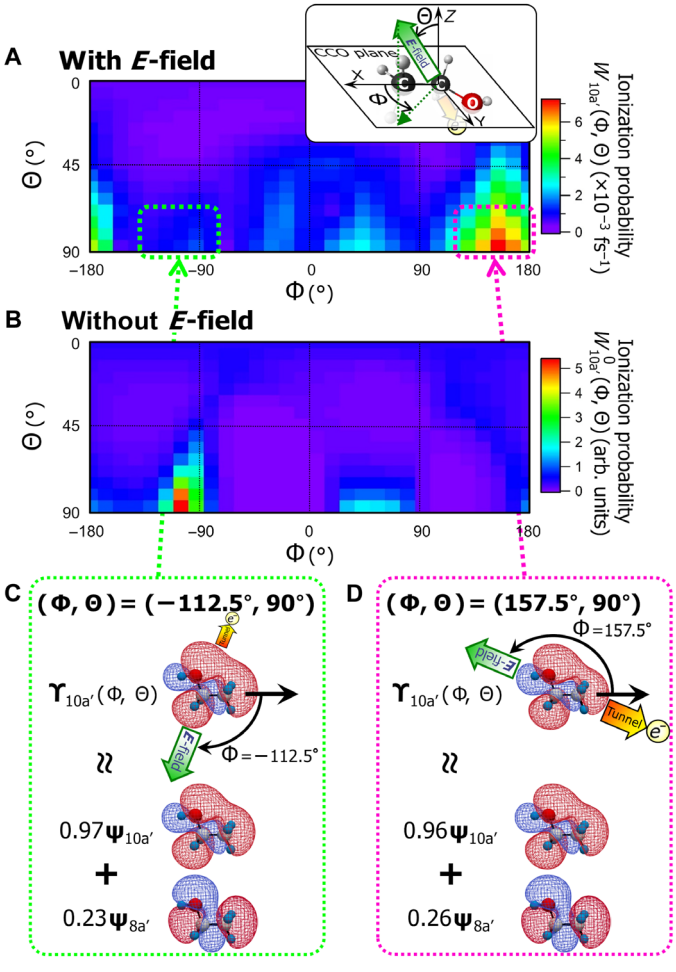

Fig. 3. MO deformation effect on the angular-dependent ionization probability. (**A**) DFT-calculated angular-dependent ionization probability of the 10a′ MO [$\Upsilon_{10a'}(\Phi, \Theta)$] in the electric field with $E = 1.7 \times 10^{10}$ V/m. Inset: Defined electric field direction represented with Euler angles (Φ, Θ). (**B**) Same as (A) but simulated for the field-free 10a′ MO ($\Psi_{10a'}$). arb. units., arbitrary units. (**C** and **D**) Field-deformed MOs $\Upsilon_{10a'}(\Phi, \Theta)$ represented by linear combinations of the field-free MOs $\Psi_{10a'}$ and $\Psi_{8a'}$ at $(\Phi, \Theta) = (-112.5°, 90°)$ and $(157.5°, 90°)$, respectively.

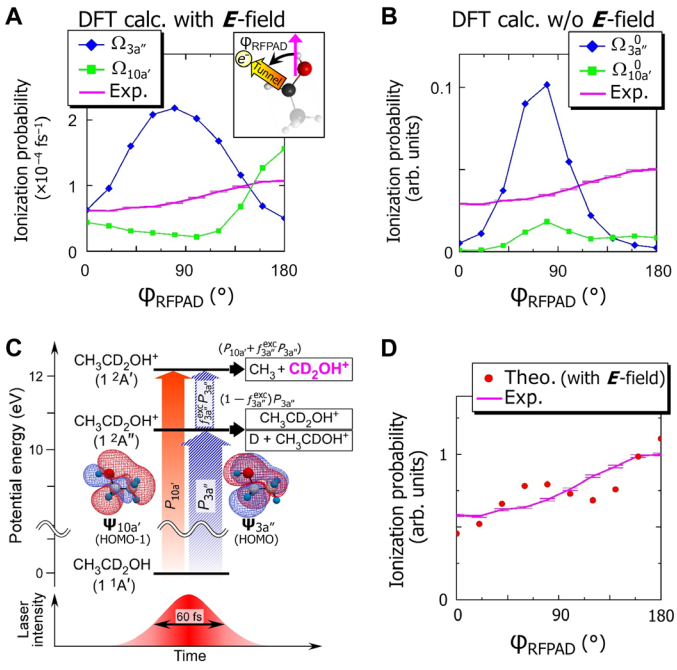

Fig. 4. Comparison of theoretical and experimental RFPADs. (**A**) Theoretical RFPADs $\Omega_{3a''}(\varphi_{RFPAD})$ and $\Omega_{10a'}(\varphi_{RFPAD})$ from field-deformed $\Upsilon_{3a''}(\Phi, \Theta)$ and $\Upsilon_{10a'}(\Phi, \Theta)$, respectively, in the electric field with $E = 1.7 \times 10^{10}$ V/m. The experimental (exp.) RFPAD is also shown with its vertical error bars. DFT calc., DFT calculations. (**B**) Same as (A) but simulated for the field-free MOs. (**C**) Schematic for the tunnel ionization and subsequent processes of CH_3CD_2OH in the circularly polarized laser field. (**D**) Comparison of the experimental RFPAD with the linear combination of the theoretical (theo.) RFPADs from the field-deformed MOs (Eq. 1 with $f^{exc}_{3a''} = 0.48$).

ionization, the adiabaticity in neutral ethanol is maintained until an electron is emitted. Structural deformation, which causes nonadiabatic transition at a specific structure, is also small in neutral ethanol. After electron emission, electronic excitation in intense laser fields can be described as nonadiabatic transition between the laser-driven adiabatic electronic states (*26*), in which the molecular structure can be deformed substantially because the Franck-Condon geometry is different from the equilibrium geometry in the ionic state (*27*). Thus, nonadiabatic excitation following electron tunneling plays a key role. Because of the two different pathways producing CD_2OH^+, the experimental RFPAD should be expressed as a linear combination of two pathways from 10a′ and 3a″

$$\Omega^{\mathrm{exp}}_{CD_2OH^+}(\varphi_{\mathrm{RFPAD}}) \propto \Omega_{10a'}(\varphi_{\mathrm{RFPAD}}) + f^{\mathrm{exc}}_{3a''}\,\Omega_{3a''}(\varphi_{\mathrm{RFPAD}}) \qquad (1)$$

where $f^{\mathrm{exc}}_{3a''}$ is the excitation fraction to the first excited $1\,^2A'$ state. Note that $f^{\mathrm{exc}}_{3a''}$ is independent of φ_{RFPAD} because we take the optical cycle average of the rotating ***E***-field. The minor contributions of the higher-lying $2\,^2A''$ and $2\,^2A'$ states of the ethanol cation are also neglected because the ion yield of $CH_3CD_2^+$ produced through these states (*23*) is small (section S1) and the ionization probabilities calculated for the lower-lying 2a″ (HOMO-2) and 9a′ (HOMO-3) MOs are also small (section S2).

We calculated the fraction $f^{\mathrm{exc}}_{3a''}$ using the measured ion yields of CD_2OH^+, $CH_3CD_2OH^+$ (m/z = 48), and CH_3CDOH^+ (m/z = 46) (Fig. 4C). We express the CD_2OH^+ yield $I(CD_2OH^+)$ as $I(CD_2OH^+) \propto P_{10a'} + f^{\mathrm{exc}}_{3a''}P_{3a''}$, where $P_{10a'}$ and $P_{3a''}$ are the integrated tunneling probabilities from 10a′ and 3a″. The sum of the $CH_3CD_2OH^+$ and CH_3CDOH^+ yields, both of which are correlated to the electronic ground $1\,^2A''$ state of $CH_3CD_2OH^+$ (*23*), is similarly expressed as $I(CH_3CD_2OH^+) + I(CH_3CDOH^+) \propto (1 - f^{\mathrm{exc}}_{3a''})P_{3a''}$. Consequently, we can express the fraction $f^{\mathrm{exc}}_{3a''}$ as

$$f^{\mathrm{exc}}_{3a''} = (R_{\mathrm{ion}}P_{3a''} - P_{10a'})/(1 + R_{\mathrm{ion}})P_{3a''} \qquad (2)$$

where $R_{\mathrm{ion}} = I(CD_2OH^+)/[I(CH_3CD_2OH^+) + I(CH_3CDOH^+)]$. Inserting the measured ion yield ratio R_{ion} = 1.3, we obtained $f^{\mathrm{exc}}_{3a''}$ = 0.48. Using the obtained $f^{\mathrm{exc}}_{3a''}$, the linear combination of Eq. 1 reasonably agrees with the experiment as shown in Fig. 4D. However, the RFPADs from the field-free MOs ($\Psi_{10a'}$ and $\Psi_{3a''}$) show a peak at around φ_{RFPAD} = 80° (green and blue lines in Fig. 4B), and the measured peak at $\varphi_{\mathrm{RFPAD}} \sim 180°$ (pink line) cannot be reproduced by linear combination of the two RFPADs from $\Psi_{10a'}$ and $\Psi_{3a''}$. This suggests that MO deformation is needed to explain the experimental RFPAD for the CD_2OH^+ channel. As shown in Fig. 1B, the contribution of the field-free 8a′ orbital to the deformed HOMO-1 orbital is essential for the peak at $\varphi_{\mathrm{RFPAD}} \sim 180°$. The remaining discrepancy between the theory and experiment in Fig. 4D is attributed to the deviation from the axial-recoil approximation in the CD_2OH^+ production.

An observed orientation dependence of the ionization probability has been well described by the tunnel ionization of an inner valence MO (10a′) deformed by an intense laser electric field. The MO deformation is not unique to ethanol but should occur in general, especially for polyatomic molecules with a high density of inner valence levels. The orientation dependence of the MO deformation presented in this study will open the door to direct control of electronic dynamics leading to selective bond breaking. Combining molecular orientation and a subcycle probe would serve this end.

MATERIALS AND METHODS

Experimental and analytical details

A linearly polarized Ti:Sapphire laser pulse (~60 fs, ~800 nm, and ~140 μJ) was converted into a circularly polarized pulse by passing through an achromatic quarter wave plate and was focused on an effusive ethanol beam with an off-axis parabolic mirror (f = 200 mm). The effusive beam of deuterated ethanol CH_3CD_2OH vapor was continuously supplied into a vacuum chamber through a microsyringe (70-μm inner diameter) and a skimmer (0.2-mm orifice diameter; Beam Dynamics model 2). The base pressure of the chamber without the sample was below 1×10^{-8} Pa.

The three-dimensional momentum vectors of an electron and an ion from an identical molecule were measured in coincidence (*18*, *21*). Ions and electrons created in the focal region were accelerated by an electrostatic lens (*28*) toward two microchannel plate detectors with delay line position encoding (RoentDek HEX80) on opposite ends of the vacuum chamber. Two-dimensional positions and time of flights were recorded using time-to-digital converters with a resolution of 25 ps (RoentDek TDC8HP). The laser repetition rate was 1 kHz, and the detection count rate was set to be less than 0.3 counts per laser shot.

The measured ion and electron momentum vectors ($\vec{\boldsymbol{p}}_{\mathrm{ion}}$ and $\vec{\boldsymbol{p}}_{\mathrm{ele}}$) were used to obtain the relative angle φ_{rel} between the projected vectors onto the polarization plane ($\vec{\boldsymbol{p}}^{\mathrm{pol}}_{\mathrm{ion}}$ and $\vec{\boldsymbol{p}}^{\mathrm{pol}}_{\mathrm{ele}}$ shown in fig. S1C). Laboratory frame electron momentum distributions have a torus shape, indicating that electrons are emitted mainly along the polarization plane (fig. S1, A and B). This electron motion suggests that the ionization proceeds in the tunnel ionization regime (*25*). RFPAD of the tunnel ionization was derived with φ_{rel} by taking account of the electron drift by the circularly polarized laser field ($\vec{\boldsymbol{p}}^{\mathrm{pol}}_{\mathrm{ele}} \perp \vec{\boldsymbol{p}}_{\mathrm{tunnel}}$). Defining φ_{rel} to be positive in going in the same direction as the ***E***-field rotation, we obtained the RFPAD as a function of $\varphi_{\mathrm{RFPAD}} = \varphi_{\mathrm{rel}} - 90°$ (fig. S1C). The laser intensity was determined by a least-squares fit to a theoretical expression of the electron momentum distribution in a circularly polarized laser field (*29*).

The laboratory frame momentum distributions of the CD_2OH^+ and $CH_3CD_2^+$ fragment ions are almost isotropic and have a peak at the center ($p_{\mathrm{ion}} = 0$) (fig. S2, A and B). The orientation of the parent molecule was determined from the direction of the fragment recoil based on the axial recoil approximation. In the present analysis, we selectively analyzed the coincidence events for the fragment ions satisfying the following two conditions. The first condition was that the out-of-plane angle of the ion emission with respect to the polarization plane was smaller than 10° ($a^{\text{out-of-plane}}_{\mathrm{ion}} < 10°$) (see also fig. S2D). This condition extracted the events producing the fragment ion recoiling along the polarization plane. The other condition concerned the fragment ion velocity υ_{ion}, which is the sum of the recoil velocity and the initial velocity of the parent molecule in the thermal distribution. The initial velocity spread of the parent molecule blurred fragment recoil direction from which the orientation of the parent molecule was determined. The velocity distribution of the parent molecule was approximated by that of the parent ion (fig. S2, A and B), because the recoil momentum [<1 atomic unit (au) as shown in fig. S1A] given by the electron tunneling and the circularly polarized laser field is smaller than the initial momentum spread of the parent ion [$\Delta p^{\mathrm{jet}}_{CH_3CD_2OH^+}$ = 14.3 au and $\Delta p^{\mathrm{TOF}}_{CH_3CD_2OH^+}$ = 2.4 au in full width at half maximum (FWHM)]. The velocity distribution indicated that most of the parent ions were slower than

2×10^{-4} au in the present experiment. Therefore, we imposed the condition of $\upsilon_{ion} \geq 2 \times 10^{-4}$ au (fig. S2, C and D).

Simulation method of tunnel ionization probability in laser electric field

The simulation procedure of the tunnel ionization probability [$W_{10a'}(\Phi, \Theta)$] is similar to the previous one (*4*). Briefly, we used the Kohn-Sham formalism in the DFT to calculate the tunnel ionization probability. Here, we considered a case in which the external field changes very slowly in time. More precisely, we assumed that the tunneling occurs much faster than one cycle of the external field. We also assumed that tunnel or above barrier processes are dominant and that the multiphoton process is negligible. Under these circumstances, the time-dependent Kohn-Sham equation (*30*) yields the static Kohn-Sham equation with an external dipole field, $V_{ext}(\vec{r}) = -e\vec{E}\cdot\vec{r}$, where E is the strength of the electric field at a certain time, as

$$\{h[n(\vec{r})] + V_{ext}(\vec{r})\}\phi_i(\vec{r}) = \epsilon_i\phi_i(\vec{r}) \tag{3}$$

Here, the electrons in the molecule are continuously emitted so that the static Kohn-Sham orbitals $\phi_i(\vec{r})$ must satisfy the outgoing boundary condition without any incident waves. This is the so-called Gamow state (*31*). Because of the outgoing boundary condition, the orbital eigenvalues, ϵ_i, are complex numbers

$$\epsilon_i = \epsilon_i^R + i\Gamma_i \tag{4}$$

where ϵ_i^R and Γ_i are the real and the imaginary parts of ϵ_i.

The imaginary part of the eigenvalue, Γ_i, is related to the ionization probability. To see it, we multiplied ϕ_i^* to Eq. 3 and subtracted its complex conjugate

$$-\frac{\hbar^2}{2m}(\phi_i^*\nabla^2\phi_i - \phi_i\nabla^2\phi_i^*) = 2i\Gamma_i|\phi_i|^2 \tag{5}$$

where m is the electron mass. We defined the current density of the ith orbital $\vec{J}_i$ as usual

$$\vec{J}_i = -\frac{i\hbar}{2m}(\phi_i^*\vec{\nabla}\phi_i - \phi_i\vec{\nabla}\phi_i^*) \tag{6}$$

Then, we found

$$\vec{\nabla}\cdot\vec{J}_i = -\frac{2}{\hbar}\Gamma_i|\phi_i|^2 \tag{7}$$

Integrating both sides over the volume V, which includes the molecule inside and using the Gauss theorem, we had

$$\int_S \vec{n}\cdot\vec{J}_i dS = -\frac{2}{\hbar}\Gamma_i\int_V |\phi_i|^2 d\vec{r} \tag{8}$$

where S is the surface of the volume V and $\vec{n}$ is a normal vector to the surface S. The ionization probability of the orbital i, w_i, is defined and is related to Γ_i as

$$w_i = \frac{\int_S \vec{n}\cdot\vec{J}_i dS}{\int_V |\phi_i|^2 d\vec{r}} = -\frac{2}{\hbar}\Gamma_i \tag{9}$$

The electrons emitted to the continuum, in principle, should contribute to the self-consistent potential. However, if the ionization probability is very small, then the contribution of emitted electrons to the potential is negligible. Under the condition that the ionization probability is sufficiently small, we calculated ionization probability through the following two steps: First, we solved the static Kohn-Sham equation under the static external field, eEz. In this step, the tunnel ionization was forced to be prohibited by placing infinite wall potential outside the barrier. The problem becomes a usual static Kohn-Sham problem except the appearance of the external dipole field and infinite wall potential. In the second step, we calculated the Gamow state solution (*31*) for each Kohn-Sham orbital using the Hamiltonian obtained at the first step with the outgoing boundary condition.

The ionization probability is sensitive to the asymptotic behavior of the potential and the binding energies of the occupied orbitals. To appropriately incorporate the asymptotic behavior, we used the exchange-correlation potential, which takes account of the self-interaction correction. We adopted an approximate construction of the optimized effective potential including the self-interaction correction, which was proposed by Krieger, Li, and Iafrate (KLI) (*32*, *33*). In this treatment, it has been shown that the ionization potentials of atoms and molecules approximately coincide with the energies of the highest occupied orbitals. The potential in this model also has a correct asymptotic behavior, $-e^2/r$, for neutral molecules, where r is the radial distance from the center of the molecule.

To calculate the Gamow states, we needed to solve the static Kohn-Sham equation (Eq. 3) with the outgoing boundary condition. For systems without spherical symmetry, the treatment of the outgoing boundary condition is not simple. Instead of imposing the outgoing boundary condition explicitly, we used the absorbing boundary condition (ABC). The absorbing potential was placed in the spatial region outside a certain radius $r = R$ with a thickness of ΔR. Outside the region of the absorbing potential, $r > R + \Delta R$, the wave functions were set to vanish. If the absorbing potential works ideally, then there exist only the outgoing waves just inside the absorbing potential.

In the present calculation, we used the following spherical absorbing potential with a linear radial dependence

$$-iW(r) = \begin{cases} 0 & (r < R) \\ -iW_0\dfrac{r-R}{R} & (R < r < R + \Delta R) \end{cases} \tag{10}$$

where R was set beyond the barrier region. As listed in table S1, we determined the height W_0 (>0) and the thickness ΔR for which the electrons coming into the region $r > R$ are absorbed completely. For the electrons with kinetic energy E_{ele}, the parameters satisfied the following condition (*34*)

$$20\frac{{E_{ele}}^{1/2}}{\Delta R\sqrt{8m}} < W_0 < \frac{1}{10}{E_{ele}}^{3/2}\sqrt{8m}\Delta R \tag{11}$$

Using the absorbing potential, the Gamow state was obtained by solving the following Kohn-Sham equation

$$\{h[n(\vec{r})] + V_{ext}(\vec{r}) - iW(\vec{r})\}\phi_i(\vec{r}) = (\epsilon_i^R + i\Gamma_i)\phi_i(\vec{r}) \tag{12}$$

with the vanishing boundary condition, $\phi_i(\vec{r}) = 0$ for $|\vec{r}| > R + \Delta R$.

We also derived an expression for the ionization probability with the absorbing potential, $W(\vec{r})$. We started with Eq. 9. We took a sphere of radius R for the volume V and applied the Gauss theorem. Then, we obtained the following expression for Γ_i

$$\Gamma_i = -\frac{\int_{r>R} d\vec{r}\,|\,\phi_i\,|^2 W(\vec{r})}{\int_{r<R} d\vec{r}\,|\,\phi_i\,|^2} \tag{13}$$

We assumed that the denominator of Eq. 13 is equal to a normalization constant, unity, so long as the ionization probability is sufficiently small. Then, the ionization probability of the orbital i is expressed as the following integral form using the absorbing potential $W(\vec{r})$ and the electron density $n_i^{\mathrm{ele}}(\vec{r}) = |\phi_i(\vec{r})|^2$

$$w_i = \frac{2}{\hbar}\int_{r>R} d\vec{r}\; n_i^{\mathrm{ele}}(\vec{r}) W(\vec{r}) \tag{14}$$

We checked whether the ionization probabilities calculated with Eq. 14 coincide with those obtained from the imaginary part of the eigenvalue within the numerical error.

To express the orbital wave functions, we used the real-space grid method. This is a convenient representation in the Kohn-Sham theory, since the potential is almost local in the coordinate representation. To impose the ABC, one must treat large spatial region far outside the molecule. The number of grid points becomes substantially large. To save the computational effort, we reduced the number of grid points using the adaptive grid.

The adaptive grid was generated as follows. We introduced the following coordinate transformation from (x, y, z) to (u, v, w) for each Cartesian coordinate

$$x = \frac{ku}{1 + (k-1)\left(\frac{u}{a\sinh(u/a)}\right)^l} \tag{15}$$

$$y = \frac{kv}{1 + (k-1)\left(\frac{v}{a\sinh(v/a)}\right)^l} \tag{16}$$

$$z = \frac{kw}{1 + (k-1)\left(\frac{w}{a\sinh(w/a)}\right)^l} \tag{17}$$

where a, k, and l determine the property of the transformation. By this transformation, there holds $x \sim u$ for small x ($x << a$) and $x \sim ku$ for large x ($x >> a$). We then discretized uniformly the variables (u, v, w) with a constant interval of h. This produced a uniform grid for small x ($x << a$) and a coarse grid for large x ($x >> a$). The transformation parameters used in the calculations are also summarized in table S1. We examined carefully that the results are not sensitive to the choice of the parameters.

Simulation method of tunnel ionization probability for field-free MO

The numerical method described in the previous section cannot be applied to the ionization probability from the undeformed MOs in the field-free condition. Instead, we evaluated the ionization probability from the number of electrons outside the potential barrier formed by the external field. We defined the potential barrier based on the Kohn-Sham potential, $V_{\mathrm{KS}} = V_{\mathrm{H}} + V_{\mathrm{xc}}$, where V_{H} is the Hartree potential and V_{xc} is the exchange-correlation potential, together with the potential by the electric field, $V_{\mathrm{ext}} = -e\vec{E}\cdot\vec{r}$. The position r_s was defined in the outer region of the barrier as the point where the total potential, $V_{\mathrm{KS}} + V_{\mathrm{ext}} + V_{\mathrm{ion}}$, where V_{ion} is the pseudopotential of ions (*35*, *36*), is equal to the binding energy of each MO. We estimated the ionization probability from the summation of the electron density outside the plane orthogonal to the electric field at $r = r_s$.

The present DFT calculation of the field-free MO was based on the same procedure used for the calculation of the molecule in the ***E***-field. We used the static Kohn-Sham formalism in the DFT without an external dipole field, which is expressed in Eq. 3 with $V_{\mathrm{ext}}(\vec{r}) = 0$. We solved the static Kohn-Sham equation with the optimized effective potential including the KLI self-interaction correction (*32*, *33*) to obtain each Kohn-Sham orbital. Each orbital wave function was expressed using the same adaptive grid represented in Eqs. 15 to 17.

Derivation of theoretical RFPAD and integrated probability from angular-dependent ionization probability

We considered three vectors of the laser electric field $\vec{E}$, the momenta of the tunneled electron $\vec{p}_{\mathrm{tunnel}}$, and recoil ion $\vec{p}_{\mathrm{ion}}$. As an initial coordinate, we took a laboratory frame (X_{L}, Y_{L}, Z_{L}), where the Z_{L} axis is parallel to the propagation direction of the laser field and the ***E***-field rotates in the $X_{\mathrm{L}}Y_{\mathrm{L}}$ plane with the azimuth angle Φ_{L} (fig. S4A). Assuming that the electron tunnels in the direction opposite to the ***E***-field, the tunneling direction is defined only by the azimuth angle φ_{L}, which fulfills the condition of $\varphi_{\mathrm{L}} = \Phi_{\mathrm{L}} + 180°$ (fig. S4A). The orientation of the ethanol molecule is defined by the Euler angles (α, β, γ) relating the laboratory frame (X_{L}, Y_{L}, Z_{L}) shown in fig. S4A and the molecular-recoil frame (X_{MR}, Y_{MR}, Z_{MR}) shown in fig. S4C, where the Z_{MR} axis is parallel to $\vec{p}_{\mathrm{ion}}$ and the C—C—O plane is on the $X_{\mathrm{MR}}Z_{\mathrm{MR}}$ plane. Here, Φ_{LR} and φ_{RFPAD} are defined as the angles of the ***E***-field and electron tunneling directions, respectively, from X_{LR} axis in the laboratory recoil frame (X_{LR}, Y_{LR}, Z_{LR}) (fig. S4B), which is obtained by the coordinate rotation represented with the direct cosine matrix $\mathbf{A}(\alpha, 0°, 0°)$ (*37*). In the laboratory recoil frame, β and γ determine the three-dimensional molecular orientation without any ambiguity. Thus, the probability of the electron tunneling as a function of φ_{RFPAD} ($=\Phi_{\mathrm{LR}} + 180°$) is described as

$$\Omega_{10a'}(\varphi_{\mathrm{RFPAD}}) = \int_0^{2\pi} d\gamma \int_{\frac{\pi}{2}-\Delta\beta}^{\frac{\pi}{2}+\Delta\beta} d\beta \sin\beta P_E(\Phi_{\mathrm{LR}}) P_{\mathrm{mol}}(\beta,\gamma)\sigma_{10a'}(\Phi_{\mathrm{LR}},\beta,\gamma) \tag{18}$$

where $P_E(\Phi_{\mathrm{LR}})$ is the probability of the ***E***-field direction, for which we substituted $1/(2\pi)$ because the laser pulse duration is long enough for the ***E***-field to be equally distributed in the polarization plane; $P_{\mathrm{mol}}(\beta, \gamma)$ is the probability of the molecular orientation direction, for which we substituted $1/(4\pi)$ because the ethanol molecules are randomly oriented with respect to β and γ. The integral with respect to β is limited by the small out-of-plane angle $\Delta\beta$ (=10°) (fig. S2D).

The ionization probability $\sigma_{10a'}(\Phi_{\mathrm{LR}}, \beta, \gamma)$ was obtained from the ionization probability $W_{10a'}(\Phi, \Theta)$ in the molecular frame (X, Y, Z) (fig. S4D) by two successive rotational transformations. We prepared three-dimensional grid points $(\Phi_{\mathrm{LR}}, \beta, \gamma)$ with equal intervals for the respective coordinates. The laboratory recoil frame was transformed to the molecular frame (fig. S4D) by the coordinate rotation represented with the two direct cosine matrices $\mathbf{A}(0°, \beta, \gamma)$ (fig. S4, B and C) and

$\mathbf{A}(-90°, -90°, -\eta_{CD_2OH^+})$ (fig. S4, C′ and D), in which $\eta_{CD_2OH^+}$ (=158.6°) is the angle between the recoil direction of CD_2OH^+ and the C—C (X) axis. The ionization probability $\sigma_{10a'}(\Phi_{LR}, \beta, \gamma)$ at each grid point was equal to the probability $W_{10a'}(\Phi, \Theta)$ at the transformed point in the molecular frame. We interpolated discrete data points of $W_{10a'}(\Phi, \Theta)$ calculated by the DFT to obtain the probability at the transformed point. Thus, the theoretical RFPAD $\Omega_{10a'}(\varphi_{RFPAD})$ was obtained by calculating the integral of Eq. 18.

To compare the theoretical RFPAD with the experimental one, the solid angle of the photoelectron emission was taken into account. We approximated the solid angle of photoelectron emission on the polarization plane to be the same as the out-of-plane distribution (fig. S3). The calculated RFPAD was convoluted with the Gaussian curve with its width of 31° (FWHM).

When we calculated the excitation fraction $f_{3a''}^{exc}$ expressed in Eq. 2, we used the ion yields obtained from the time-of-flight mass spectrum. Here, we could not select the ionizing molecules in the limited range of the out-of-plane angle β. The probability $P_{10a'}$ was calculated by the following integral

$$P_{10a'} = \frac{1}{8\pi^2}\int_0^{2\pi} d\Phi_{LR}\int_0^{2\pi} d\gamma\int_0^{\pi} d\beta \sin\beta\sigma_{10a'}(\Phi_{LR}, \beta, \gamma) \qquad (19)$$

Note that the analytical procedure mentioned in this section is valid not only for the 10a′ but also for all other orbitals.

SUPPLEMENTARY MATERIALS

Supplementary material for this article is available at http://advances.sciencemag.org/cgi/content/full/5/5/eaaw1885/DC1

Section S1. Yields of fragment ions produced from CH_3CD_2OH in the circularly polarized laser field

Section S2. Comparison of measured RFPAD for the $CH_3CD_2^+$ production with theoretical RFPADs

Fig. S1. Electron momentum distributions in the laboratory frame.

Fig. S2. Ion momentum distributions in the laboratory frame.

Fig. S3. Out-of-plane angular distributions of electrons with respect to the polarization plane.

Fig. S4. Scheme of the rotational transformations for derivation of theoretical RFPAD.

Fig. S5. Time-of-flight mass spectrum of CH_3CD_2OH.

Fig. S6. Results for the $CH_3CD_2^+$ production channel.

Table S1. The spatial parameters used in the calculations of ethanol.

REFERENCES AND NOTES

1. K. Fukui, T. Yonezawa, H. Shingu, A molecular orbital theory of reactivity in aromatic hydrocarbons. *J. Chem. Phys.* **20**, 722–725 (1952).
2. R. Hoffmann, R. B. Woodward, Orbital symmetry control of chemical reactions. *Science* **167**, 825–831 (1970).
3. X. M. Tong, Z. X. Zhao, C. D. Lin, Theory of molecular tunneling ionization. *Phys. Rev. A* **66**, 033402 (2002).
4. T. Otobe, K. Yabana, J.-I. Iwata, First-principles calculations for the tunnel ionization rate of atoms and molecules. *Phys. Rev. A* **69**, 053404 (2004).
5. A. S. Alnaser, S. Voss, X.-M. Tong, C. M. Maharjan, P. Ranitovic, B. Ulrich, T. Osipov, B. Shan, Z. Chang, C. L. Cocke, Effects of molecular structure on ion disintegration patterns in ionization of O_2 and N_2 by short laser pulses. *Phys. Rev. Lett.* **93**, 113003 (2004).
6. D. Pavičić, K. F. Lee, D. M. Rayner, P. B. Corkum, D. M. Villeneuve, Direct measurement of the angular dependence of ionization for N_2, O_2, and CO_2 in intense laser fields. *Phys. Rev. Lett.* **98**, 243001 (2007).
7. L. Holmegaard, J. L. Hansen, L. Kalhøj, S. L. Kragh, H. Stapelfeldt, F. Filsinger, J. Küpper, G. Meijer, D. Dimitrovski, M. Abu-samha, C. P. J. Martiny, L. B. Madsen, Photoelectron angular distributions from strong-field ionization of oriented molecules. *Nat. Phys.* **6**, 428–432 (2010).
8. M. Meckel, D. Comtois, D. Zeidler, A. Staudte, D. Pavičić, H. C. Bandulet, H. Pépin, J. C. Kieffer, R. Dörner, D. M. Villeneuve, P. B. Corkum, Laser-induced electron tunneling and diffraction. *Science* **320**, 1478–1482 (2008).
9. H. Akagi, T. Otobe, A. Staudte, A. Shiner, F. Turner, R. Dörner, D. M. Villeneuve, P. B. Corkum, Laser tunnel ionization from multiple orbitals in HCl. *Science* **325**, 1364–1367 (2009).
10. B. K. McFarland, J. P. Farrell, P. H. Bucksbaum, M. Gühr, High harmonic generation from multiple orbitals in N_2. *Science* **322**, 1232–1235 (2008).
11. O. Smirnova, Y. Mairesse, S. Patchkovskii, N. Dudovich, D. Villeneuve, P. Corkum, M. Y. Ivanov, High harmonic interferometry of multi-electron dynamics in molecules. *Nature* **460**, 972–977 (2009).
12. M. D. Śpiewanowski, L. B. Madsen, Alignment- and orientation-dependent strong-field ionization of molecules: Field-induced orbital distortion effects. *Phys. Rev. A* **91**, 043406 (2015).
13. M. D. Śpiewanowski, A. Etches, L. B. Madsen, High-order-harmonic generation from field-distorted orbitals. *Phys. Rev. A* **87**, 043424 (2013).
14. P. M. Kraus, O. I. Tolstikhin, D. Baykusheva, A. Rupenyan, J. Schneider, C. Z. Bisgaard, T. Morishita, F. Jensen, L. B. Madsen, H. J. Wörner, Observation of laser-induced electronic structure in oriented polyatomic molecules. *Nat. Commun.* **6**, 7039 (2015).
15. B. Jochim, R. Siemering, M. Zohrabi, O. Voznyuk, J. B. Mahowald, D. G. Schmitz, K. J. Betsch, B. Berry, T. Severt, N. G. Kling, T. G. Burwitz, K. D. Carnes, M. F. Kling, I. Ben-Itzhak, E. Wells, R. de Vivie-Riedle, The importance of Rydberg orbitals in dissociative ionization of small hydrocarbon molecules in intense laser fields. *Sci. Rep.* **7**, 4441 (2017).
16. M. F. Kling, C. Siedschlag, A. J. Verhoef, J. I. Khan, M. Schultze, T. Uphues, Y. Ni, M. Uiberacker, M. Drescher, F. Krausz, M. J. J. Vrakking, Control of electron localization in molecular dissociation. *Science* **312**, 246–248 (2006).
17. P. M. Kraus, B. Mignolet, D. Baykusheva, A. Rupenyan, L. Horný, E. F. Penka, G. Grassi, O. I. Tolstikhin, J. Schneider, F. Jensen, L. B. Madsen, A. D. Bandrauk, F. Remacle, H. J. Wörner, Measurement and laser control of attosecond charge migration in ionized iodoacetylene. *Science* **350**, 790–795 (2015).
18. K. Hosaka, R. Itakura, K. Yokoyama, K. Yamanouchi, A. Yokoyama, Photoelectron–photoion coincidence momentum imaging for dissociative ionization of ethanol in intense laser fields. *Chem. Phys. Lett.* **475**, 19–23 (2009).
19. T. Ikuta, K. Hosaka, H. Akagi, A. Yokoyama, K. Yamanouchi, F. Kannari, R. Itakura, Separation of ionization and subsequent electronic excitation for formation of electronically excited ethanol cation in intense laser fields. *J. Phys. B: At., Mol. Opt. Phys.* **44**, 191002 (2011).
20. A. E. Boguslavskiy, J. Mikosch, A. Gijsbertsen, M. Spanner, S. Patchkovskii, N. Gador, M. J. J. Vrakking, A. Stolow, The multielectron ionization dynamics underlying attosecond strong-field spectroscopies. *Science* **335**, 1336–1340 (2012).
21. K. Hosaka, A. Yokoyama, K. Yamanouchi, R. Itakura, Correlation between a photoelectron and a fragment ion in dissociative ionization of ethanol in intense near-infrared laser fields. *J. Chem. Phys.* **138**, 204301 (2013).
22. M. B. Robin, N. A. Kuebler, Excited electronic states of the simple alcohols. *J. Electron Spectrosc. Relat. Phenom.* **1**, 13–28 (1973).
23. Y. Niwa, T. Nishimura, T. Tsuchiya, Ionic dissociation of ethanol studied by photoelectron—Photoion coincidence spectroscopy. *Int. J. Mass Spectrom. Ion Phys.* **42**, 91–99 (1982).
24. A. Staudte, S. Patchkovskii, D. Pavičić, H. Akagi, O. Smirnova, D. Zeidler, M. Meckel, D. M. Villeneuve, R. Dörner, M. Y. Ivanov, P. B. Corkum, Angular tunneling ionization probability of fixed-in-space H_2 molecules in intense laser pulses. *Phys. Rev. Lett.* **102**, 033004 (2009).
25. P. B. Corkum, N. H. Burnett, F. Brunel, Above-threshold ionization in the long-wavelength limit. *Phys. Rev. Lett.* **62**, 1259–1262 (1989).
26. M. Lezius, V. Blanchet, M. Y. Ivanov, A. Stolow, Polyatomic molecules in strong laser fields: Nonadiabatic multielectron dynamics. *J. Chem. Phys.* **117**, 1575–1588 (2002).
27. H. Kono, Y. Sato, M. Kanno, K. Nakai, T. Kato, Theoretical investigations of the electronic and nuclear dynamics of molecules in intense laser fields: Quantum mechanical wave packet approaches. *Bull. Chem. Soc. Jpn.* **79**, 196–227 (2006).
28. M. Lebech, J. C. Houver, D. Dowek, Ion-electron velocity vector correlations in dissociative photoionization of simple molecules using electrostatic lenses. *Rev. Sci. Instrum.* **73**, 1866–1874 (2002).
29. N. B. Delone, V. P. Krainov, Tunneling and barrier-suppression ionization of atoms and ions in a laser radiation field. *Phys.-Usp.* **41**, 469–485 (1998).
30. W. Kohn, L. J. Sham, Self-consistent equations including exchange and correlation effects. *Phys. Rev.* **140**, A1133–A1138 (1965).
31. G. Gamow, Zur quantentheorie des atomkernes. *Z. Phys.* **51**, 204–212 (1928).
32. J. B. Krieger, Y. Li, G. J. Iafrate, Construction and application of an accurate local spin-polarized Kohn-Sham potential with integer discontinuity: Exchange-only theory. *Phys. Rev. A* **45**, 101–126 (1992).
33. X.-M. Tong, S.-I. Chu, Density-functional theory with optimized effective potential and self-interaction correction for ground states and autoionizing resonances. *Phys. Rev. A* **55**, 3406–3416 (1997).
34. T. Nakatsukasa, K. Yabana, Photoabsorption spectra in the continuum of molecules and atomic clusters. *J. Chem. Phys.* **114**, 2550–2561 (2001).
35. L. Kleinman, D. M. Bylander, Efficacious form for model pseudopotentials. *Phys. Rev. Lett.* **48**, 1425–1428 (1982).

36. N. Troullier, J. L. Martins, Efficient pseudopotentials for plane-wave calculations. *Phys. Rev. B* **43**, 1993–2006 (1991).
37. R. N. Zare, *Angular Momentum: Understanding Spatial Aspects in Chemistry and Physics* (Baker Lecture Series, Wiley-Interscience, 1998).

Acknowledgments: We thank K. Hosaka, K. Yamanouchi, and A. Yokoyama for support in developing the PEPICO apparatus, Y. Hagihara for support in data analysis, and H. Kono and M. Tsubouchi for valuable discussions. **Funding:** We acknowledge valuable financial support from JSPS KAKENHI grant numbers JP22685004, JP23350013, JP26288013, and JP17H03525. **Author contributions:** H.A. and R.I. conceived and designed this study. R.I. developed the laser system and PEPICO apparatus. H.A. conducted the experiments and analyzed the measured data. T.O. performed the ab initio calculations and provided the theoretical interpretation. R.I. made the comparison between experimental and theoretical RFPAD and supervised the project. H.A. drafted the original manuscript, and all authors edited and reviewed the manuscript. **Competing interests:** The authors declare that they have no competing interests. **Data and materials availability:** All data needed to evaluate the conclusions in the paper are present in the paper and/or the Supplementary Materials. Additional data related to this paper may be requested from the authors.

Submitted 27 November 2018
Accepted 2 April 2019
Published 17 May 2019
10.1126/sciadv.aaw1885

Citation: H. Akagi, T. Otobe, R. Itakura, Deformation of an inner valence molecular orbital in ethanol by an intense laser field. *Sci. Adv.* **5**, eaaw1885 (2019).